Confinement of long-lived interlayer excitons in WS_2/WSe_2 heterostructures

Alejandro R.-P. Montblanch,[1,*] Dhiren M. Kara,[1,*] Ioannis Paradisanos,[2] Carola M. Purser,[1,2] Matthew S. G. Feuer,[1] Evgeny M. Alexeev,[2,1] Lucio Stefan,[1,3] Ying Qin,[4] Mark Blei,[4] Gang Wang,[2] Alisson R. Cadore,[2] Pawel Latawiec,[5] Marko Lončar,[5] Sefaattin Tongay,[4] Andrea C. Ferrari,[2,†] and Mete Atatüre[1,‡]

[1]*Cavendish Laboratory, University of Cambridge, 19 J. J. Thomson Ave., Cambridge, CB3 0HE, UK*

[2]*Cambridge Graphene Centre, University of Cambridge, 9 J. J. Thomson Ave., Cambridge, CB3 0FA, UK*

[3]*The Faraday Institution, Quad One, Becquerel Avenue, Harwell Campus, Didcot, OX11 0RA, UK*

[4]*School for Engineering of Matter, Transport and Energy, Arizona State University, Tempe, AZ, 85287, USA*

[5]*School of Engineering and Applied Science, Harvard University, Cambridge, MA, 02138, USA*

Abstract

Interlayer excitons in layered materials constitute a novel platform to study many-body phenomena arising from long-range interactions between quantum particles. The ability to localise individual interlayer excitons in potential energy traps is a key step towards simulating Hubbard physics in artificial lattices. Here, we demonstrate spatial localisation of long-lived interlayer excitons in a strongly confining trap array using a WS_2/WSe_2 heterostructure on a nano-patterned substrate. We detect long-lived interlayer excitons with lifetime approaching 0.2 ms and show that their confinement results in a reduced lifetime in the microsecond range and stronger emission rate with sustained optical selection rules. The combination of a permanent dipole moment, spatial confinement and long lifetime places interlayer excitons in a regime that satisfies one of the requirements for observing long-range dynamics in an optically resolvable trap lattice.

[*] These two authors contributed equally.

[†] acf26@cam.ac.uk

[‡] ma424@cam.ac.uk

Since the demonstration of Bose-Einstein condensation[1, 2], ultracold atoms have played a central role in the study and realization of macroscopic-scale quantum phenomena, including Mott transition[3], superfluidity[4] and many-body localisation[5]. In parallel, exciton-polaritons have become an equivalent platform in semiconductors[6–12]. Recently, dipolar particles have gained attention as they introduce long-range anisotropic interactions to the exploration of new states of quantum matter[13–15]. Atomic realizations of dipolar ensembles include Rydberg atoms[16–18], ultracold polar molecules[19–21] and high magnetic-moment atoms[22–26]. For semiconductors, long-range interactions can be achieved via spatially indirect excitons, where electrons and holes have finite separation[27, 28] yielding a permanent electric dipole moment[29–31]. Most progress in realizing such states has been in AlGaAs/GaAs double quantum wells[30, 32–35], while heterostructures of transition metal dichalcogenide (TMD) monolayers[36] have recently emerged as a promising alternative[37–40]. TMD monolayers are semiconductors offering optical access to orbital, spin and valley degrees of freedom[41], and the difference in band energies of two different TMDs is exploited to create type-II interlayer excitons[42, 43] with static electric dipole. Moreover, their optical transition strength, energy, and selection rules can be engineered by controlling the layer separation[44] and the relative stacking angle of the monolayers[45–50].

The potential of TMD interlayer excitons for many-body physics is evidenced by recent reports of exciton condensation[51] and the creation of moir lattices for exploring Hubbard[52] and Mott[53, 54] physics. While a moir lattice achieved through angled stacking of TMD monolayers is an exciting route, the typical lattice constant is restricted to a few nanometres, well below the optical diffraction limit ($\sim$0.5 μm), preventing single-site optical access. Trapping interlayer excitons in an independent potential energy landscape offers a solid-state analogue of atoms in single-site addressable optical lattices[55, 56], and first indications of confined interlayer excitons were reported recently[57, 58]. An elementary requirement for long-range interactions to manifest in such systems is that the interlayer exciton decay rate is smaller than the dipole-dipole coupling rate in neighbouring lattice sites. For TMD interlayer excitons, shown to have an electric dipole of $\sim$0.6 e·nm ($\sim$29 Debye)[40], the dipole-dipole coupling rate at a distance of $\sim$0.5 μm is 1 MHz[59]. This means that a trapped interlayer exciton lifetime of at least one microsecond needs to be achieved.

Figure 1a is an illustration of our device, fabricated by exfoliating WSe_2 and WS_2 monolayers from bulk crystals and transferring these onto a SiO_2/Si substrate patterned with

an array of nanopillars 220-250 nm tall and 4 μm apart (see Methods and Section 1 of the Supplementary Information, SI). We choose an interlayer stacking angle of ~50, away from high-symmetry angles of 0 or 60, in order to introduce an interlayer momentum mismatch to reduce the exciton recombination rate. Five distinct locations are labelled in Fig. 1a as L1-L5. These locations are marked by circles in the optical image of our device shown in Fig. 1b, where the WSe_2 and WS_2 monolayers are outlined in red and green, respectively, yielding a large region (>160 μm^2) of the WS_2/WSe_2 heterobilayer.

Figure 1c shows a photoluminescence (PL) map taken with continuous-wave (CW) 2.33-eV (532-nm) laser excitation at a temperature T=4 K. This energy is greater than both the WSe_2 and WS_2 optical bandgaps of 1.73 eV[60] and 2.08 eV[61], respectively. Consequently, PL emission is observed from both monolayer and heterobilayer regions. The spectral emission from the flat monolayer regions (L1 and L2 in Fig. 1b) is shown in Figs. 1d (i) and (ii), respectively. The PL emission between 1.65 and 2.0 eV in panel (i) (filled in green) is the intralayer exciton recombination in monolayer WS_2[61, 62], and that between 1.6 and 1.75 eV in panel (ii) (filled in red) is the intralayer exciton recombination in monolayer WSe_2[60, 63]. Figure 1d panel (iii) shows the spectrum from the flat part of the heterobilayer, L3 in Fig. 1b. A lower-energy feature around 1.4 eV (filled in yellow) is consistent with interlayer exciton emission from stacked WS_2/WSe_2 heterobilayers reported previously[50, 64]. Figure 1d (iv) is the PL spectrum from a monolayer WSe_2 on a nanopillar, presented as reference, displaying a ~50-fold brighter emission with respect to flat monolayer WSe_2 and a sub-meV full-width at half-maximum spectral peak. Given that monolayer WSe_2 on such nanopillars results in the strong quantum confinement of intralayer excitons[62, 65], we look for similar signatures in the interlayer emission spectra. Figure 1d (v) is the PL spectrum of the heterobilayer on a nanopillar. We observe a 20-fold brighter interlayer emission in the low optical excitation regime (below 1 μW) and sharp spectral features (~1 meV full-width at half-maximum), in contrast to the weak and spectrally broad emission from the flat heterobilayer.

To isolate interlayer excitations from any effects coming from the monolayers, such as free charge carriers or intralayer excitons, we use an optical excitation energy of 1.50 eV for all other measurements. This energy is at the onset of the interlayer exciton PL spectrum, Fig. 1d (iii), and below the optical bandgap energies of WSe_2 and WS_2 monolayers. Figure 1e displays the PL intensity map of our device under 1.50-eV excitation. The emission is

only observed from the heterobilayer region with both monolayer regions remaining dark, demonstrating that only interlayer excitons are generated, as anticipated.

Figure 2a shows the interlayer exciton PL spectra from the flat heterobilayer for 0.05-μW (black curve), 1-μW (red curve) and 100-μW (blue curve) laser excitation power, P, at T=4 K. The spectrally integrated PL intensity of interlayer exciton with respect to P is shown in Fig. 2b. While the interlayer exciton emission starts with a linear dependence on P, it converges to a $P^{0.3}$ scaling for P>0.3 μW. Sublinear behaviour was also reported for $MoSe_2/WSe_2$ heterobilayers[36]. This can be caused by density-dependent mechanisms such as exciton-exciton annihilation, dipolar repulsion and phase-space filling.

Figure 2c presents PL spectra from the heterobilayer on a nanopillar for P =0.05 μW (black curve), 1 μW (red curve) and 100 μW (blue curve). With increasing power the three peaks highlighted in green, grey and blue saturate. The integrated PL intensity as a function of P from these peaks are plotted in Fig. 2d, with data (squares) colour-coded for the highlighted peaks of Fig. 2c. Each shows a linear P -dependence, followed by saturation. This behaviour is characteristic of a quantum-confined system[66, 67], and contrasts that of untrapped interlayer excitons in the flat heterobilayer (Figs. 2a and b). Eight nanopillar locations display this saturating behaviour (Fig. S3a in SI), demonstrating that interlayer-exciton trapping is reproduced across the device.

Figures 3a and 3b present trapped interlayer exciton PL spectra above a nanopillar (L5 of Fig. 1b) at T=4 K, for out-of-plane magnetic field B from 0 to 9 T. In panel a (panel b) the excitation is linearly polarised and the collection is right-hand σ^+ (left-hand σ^-) circularly polarised. The red-shifting Zeeman state from each emission line is only seen for σ^+ detection, while the blue-shifting Zeeman state is only seen for σ^- detection. This demonstrates that the two magnetic configurations of trapped interlayer excitons have sustained optical selection rules[68].

The distribution of Zeeman splitting with respect to B across different nanopillars is given in Fig. 3c as a blue-shaded region, where the data corresponding to the smallest and largest measured g-factor (11.9 and 15.4) are plotted in blue and red circles, respectively. The similarity in g-factors, mean value 13.2±1.1, across the nanopillar traps and for different PL peaks (Fig. S3b in SI) suggests that the trapped excitons have the same microscopic origin. The variation in g-factors is also similar to that observed in confined intralayer excitons in WSe_2 monolayers[67, 70–72]. This contrasts the order of magnitude smaller distribution in g-

factor observed for trapped interlayer excitons in homogeneous moir trapping potentials[49].

Figure 3d presents the PL spectra under σ^+ excitation at B =0 T for σ^+ (black) and σ^- (red) circularly polarised collection. The overlap of the two spectra demonstrates that excitation polarisation is not maintained for trapped interlayer excitons. One dominant mechanism for this loss of polarisation is the exchange interaction between bound electron and holes[73]. For trapped interlayer excitons the exchange interaction rate and the exciton decay rate should be reduced proportionally with the increased electron-hole separation, but the exciton decay rate is additionally suppressed when the momentum-space overlap is reduced, as expected for heterobilayers with a stacking angle not matching 0 or 60[48].

Figure 4 presents lifetime measurements on interlayer excitons under pulsed (~3-ps pulse duration) laser excitation at 1.50 eV at T=4 K (see Methods). Figure 4a shows an example emission intensity histogram of untrapped interlayer excitons (grey bars) as a function of time after excitation, and an exponential fit (solid red curve) reveals a decay time of 180.6±3.5 μs. Across the flat heterobilayer region, the average lifetime is 175±5 μs. Since only interlayer excitons are created under 1.50 eV excitation, spuriously prolonged lifetimes resulting from the delayed capture of free carriers[74] or higher energy intralayer dark excitons[75] are avoided. The spatial and momentum separation of electrons and holes of interlayer excitons, and the use of high-quality monolayers (see Methods), are likely responsible for these values. That said, this lifetime shows a strong excitation dependence: increasing the excitation power reduces the exciton decay time (Fig. S4 in SI), as expected from density-dependent interactions and loss channels, even in the regime where PL intensity depends linearly on the excitation power (P<0.3 μW in Fig. 2b).

Figure 4b is a lifetime measurement of the trapped interlayer exciton spectral line at 1.39 eV from Fig. 3d (L5 in Fig. 1b). We fit a biexponential function of the form $A_s e^{-t/\tau_s} + A_l e^{-t/\tau_l}$, where τ_l (τ_s) is the long (short) lifetime and A_l (A_s) is the amplitude of the exponential with long (short) lifetime. This yields τ_s =59.4±0.9 ns and τ_l =389.1±1.2 ns. This biexponential behaviour, albeit with varying lifetimes, is observed throughout the entire spectral range for trapped interlayer excitons (Fig. S5 in SI). Figure 4c is a summary of the spectrally integrated lifetimes from the eight nanopillar traps. The extracted τ_s and τ_l values are shown in Fig. 4c in black and grey bars, and lie in the ~10-175 ns and ~0.4-4 μs ranges, respectively. The reduction in the interlayer exciton lifetime after trapping accompanies an enhancement in PL brightness, suggesting a modified oscillator strength under

localisation. This likely arises from the relaxation of stacking-angle-induced momentum mismatch on nanopillars, that otherwise inhibits the recombination of untrapped interlayer excitons[76]. One possible origin of the observed biexponential decay is the presence of two excited states: an optically active state and an energetically similar shelving state (inset diagram in Fig. 4b). A three-level model combined with temperature-dependent measurements (Section 5 in SI) yields average radiative and non-radiative recombination rates of trapped interlayer excitons across the nanopillar sites $1/\tau_s \approx \Gamma_r \approx 13$ MHz and $1/\tau_l \approx \Gamma_{nr} \approx 500$ kHz, respectively. This reveals the considerably smaller average non-radiative decay rate and indicates that the long-lived shelving state decays primarily through radiative emission. Temperature-dependent measurements demonstrate that thermal excitations also couple bright and shelving states as evidenced in Fig. S6d of SI.

The spatial trapping we show here is a first step towards building arrays of long-lived and interacting interlayer excitons. Our trapped interlayer exciton lifetime, ~4 μs, is sufficient to observe dipole-mediated exciton interactions for an optically resolvable lattice spacing of ~0.5 μm. The immediate next step is to develop a full account of the photophysics of these trapped interlayer excitons, including the influence of stacking angle, interlayer spacing, electrostatic gating of the heterobilayer, and resonant excitation. In addition, other trapping geometries, such as ridges and rings, can offer the opportunity to probe many-body phenomena in one dimension.

I. ACKNOWLEDGEMENTS

We acknowledge funding from the EU Quantum Technology (2D-SIPC) and Graphene Flagships; ERC grants PEGASOS, Hetero2D and GSYNCOR; EPSRC Grants EP/K01711X/1, EP/K017144/1, EP/N010345/1 and EP/L016057/1; and the Faraday Institution FIRG001. D. M. K. acknowledges support of a Royal Society university research fellowship URF¥R1¥180593. S.T. acknowledges support from DOE, NSF DMR 1552220, DMR 1904716, and NSF CMMI 1933214.

II. METHODS

A. Fabrication

Van der Waals TMD bulk crystals were synthesised through flux zone growth technique[77]. Precursor powders were purchased from commercial vendors (Alfa Aesar) but additional electrolytic purification process was implemented to achieve 99.9999% or higher purity. After the purification these powders were analysed using secondary ion mass spectroscopy to confirm absence of metal impurities. Compared to crystals grown by chemical vapour transport, flux grown ones were free of point defects and topological defects.

Flakes are then prepared by micromechanical cleavage[78] on Nitto Denko tape, then exfoliated again for transfer to a polydimethylsiloxane (PDMS) stamp placed on a transparent glass slide, allowing bidirectional inspection of the flakes under the optical microscope. Optical contrast is utilized to identify monolayers prior to transfer[79]. We get monolayer flakes with lateral dimensions ~50 μm. Substrates with arrays of silica nanopillars, 100 nm in diameter and 220-250 nm high are prepared by direct-write lithography[62]. The substrates undergo wet cleaning (1-minute ultrasonication in acetone and isopropanol) and are subsequently exposed to an oxygen-assisted plasma at a power of 10 W for 60 s to remove impurities and contaminants from the surface. The WSe_2 monolayer is then stamped on the nanopillars with a micro-manipulator [62, 80]. After the first transfer, the second (WS_2) monolayer is deposited on top of the WSe_2 monolayer following the same stamping procedure. In both steps the PDMS stamp is removed after depositing the monolayer. Raman (Fig. S1a in SI), second-harmonic generation (Fig. S1b in SI) and atomic force microscopy (Fig. S2 in SI) measurements confirm the monolayer nature of the constituents, the twist angle and the interlayer spacing, respectively.

B. Photoluminescence measurements

All PL measurements are done at T=4 K in a 9-T closed-cycle cryostat (Attocube). Excitation and collection pass through a home-built confocal setup with the sample in reflection geometry. CW illumination from either a 2.33 eV laser (Ventus) or a Ti:Sapphire laser (Mira 900) at 1.58 or 1.50 eV is used. The PL signal is spectrally filtered and sent to a 150-line grating spectrometer (Princeton Instruments).

C. Lifetime measurements

To perform lifetime measurements, we excite the samples every few μs (up to ~10 μs for the trapped interlayer excitons, and up to 1 ms for the interlayer exciton) with ~3 ps pulses from a Ti:Sapphire laser (Mira 900) tuned to 785 nm (1.58 eV) or 825 nm (1.50 eV). An acousto-optic modulator (AOM) down-samples the 76 MHz laser repetition rate to the kHz-MHz range required to measure up to hundreds of μs lifetimes. A time-to-digital converter (QuTau) with 81 ps timing resolution collects start-stop histograms with "start" triggered by the AOM pulse-picking and "stop" triggered by an avalanche photodiode (APD) output from single-photon detection of interlayer exciton PL. The converter remains idle until a subsequent "start" signal arrives. We ensure that we are not susceptible to spurious artefacts from start-stop measurements by measuring lifetime at a subset of locations using photon time-tagging and calculating lifetimes in post-processing. Both methods result in consistent lifetimes for trapped interlayer excitons, but time-tagging is required for the measurement of the unbound interlayer exciton lifetimes, due to its count rate being comparable to or even lower than the APD dark counts, as well as being at least one order of magnitude smaller than the pulse rate sent to the sample.

---

[1] Anderson, M. H. *et al.* Observation of Bose-Einstein Condensation in a Dilute Atomic Vapor. *Science* **269**, 198201 (1995).

[2] Davis, K. B. *et al.* Bose-Einstein Condensation in a Gas of Sodium Atoms. *Phys. Rev. Lett.* **75**, 39693973 (1995).

[3] Greiner, M. *et al.* Quantum phase transition from a superfluid to a Mott insulator in a gas of ultracold atoms. *Nature* **415**, 39 (2002).

[4] Zwierlein, M. W. *et al.* Vortices and superfluidity in a strongly interacting Fermi gas. *Nature* **435**, 10471051 (2005).

[5] Schreiber, M. *et al.* Observation of many-body localization of interacting fermions in a quasir-andom optical lattice. *Science* **349**, 842-845 (2015).

[6] Deng, H. *et al.* Condensation of semiconductor microcavity exciton polaritons. *Science* **298**, 199202 (2002).

[7] Kasprzak, J. *et al.* Bose-Einstein condensation of exciton polaritons. *Nature* **443**, 40914 (2006).

[8] Balili, R. *et al.* Bose-Einstein condensation of microcavity polaritons in a trap. *Science* **316**, 10071010 (2007).

[9] Plumhof, J. D. *et al.* Room-temperature Bose-Einstein condensation of cavity exciton-polaritons in a polymer. *Nat. Mater.* **13**, 247 (2013).

[10] Byrnes, T. *et al.* Exciton-polariton condensates. *Nat. Phys.* **10**, 803 (2014).

[11] Wertz, E. *et al.* Spontaneous formation and optical manipulation of extended polariton condensates. *Nat. Phys.* **6**, 860 (2010).

[12] Amo, A. *et al.* Superfluidity of polaritons in semiconductor microcavities. *Nat. Phys.* **5**, 805 (2009).

[13] Baranov, M. A. *et al.* Condensed matter theory of dipolar quantum gases. *Chem. Rev.* **112**, 50125061 (2012).

[14] Trefzger, C. *et al.* Ultracold dipolar gases in optical lattices. *J. Phys. B: At. Mol. Opt. Phys.* **44**, 193001 (2011).

[15] Lahaye, T. *et al.* The physics of dipolar bosonic quantum gases. *Rep. Prog. Phys.* **72**, 126401 (2009).

[16] Schauss, P. *et al.* Observation of spatially ordered structures in a two-dimensional Rydberg gas. *Nature* **491**, 87 (2012).

[17] Schauss, P. *et al.* Crystallization in Ising quantum magnets. *Science* **347**, 1455 (2015).

[18] Saffman, M. *et al.* Quantum information with Rydberg atoms. *Rev. Mod. Phys.* **82**, 2313 (2010).

[19] Truppe, S. *et al.* Molecules cooled below the Doppler limit. *Nat. Phys.* **13**, 1173 (2017).

[20] Bohn, J. L. *et al.* Cold molecules: Progress in quantum engineering of chemistry and quantum matter. *Science* **357**, 1002 (2017).

[21] Carr, L. D. Cold and ultracold molecules: science, technology and applications. *New J. Phys.* **11**, 055049 (2009).

[22] Griesmaier, A. *et al.* Bose-Einstein Condensation of Chromium. *Phys. Rev. Lett.* **94**, 160401 (2005).

[23] Lu, M. *et al.* Strongly Dipolar Bose-Einstein Condensate of Dysprosium. *Phys. Rev. Lett.* **107**, 190401 (2011).

[24] Aikawa, K. *et al.* Bose-Einstein Condensation of Erbium. *Phys. Rev. Lett.* **108**, 210401 (2012).

[25] Baier, S. *et al.* Extended Bose-Hubbard models with ultracold magnetic atoms. *Science* **352**, 201 (2016).

[26] de Paz, A. *et al.* Nonequilibrium Quantum Magnetism in a Dipolar Lattice Gas. *Phys. Rev. Lett.* **111**, 185305 (2013).

[27] Chen, Y. J. *et al.* Effect of electric fields on excitons in a coupled double-quantum-well structure. *Phys. Rev. B* **36**, 4562 (1987).

[28] Golub, J. E. *et al.* Type Itype II anticrossing and enhanced Stark effect in asymmetric coupled quantum wells. *Appl. Phys. Lett.* **53**, 2584 (1988).

[29] Voros, Z. *et al.* Long-Distance Diffusion of Excitons in Double Quantum Well Structures. *Phys. Rev. Lett.* **94**, 226401 (2005).

[30] Hubert, C. *et al.* Attractive Dipolar Coupling between Stacked Exciton Fluids. *Phys. Rev. X* **9**, 021026 (2019).

[31] Hubert, C. *et al.* Attractive interactions, molecular complexes, and polarons in coupled dipolar exciton fluids. arXiv:1910.06015 (2019).

[32] Butov, L. V. *et al.* Macroscopically ordered state in an exciton system. *Nature* **418**, 751 (2002).

[33] High, A. A. *et al.* et al. Spontaneous coherence in a cold exciton gas. *Nature* **483**, 584588 (2012).

[34] Shilo, Y. *et al.* Particle correlations and evidence for dark state condensation in a cold dipolar exciton fluid. *Nat. Commun.* **4**, 2335 (2013).

[35] Stern, M. *et al.* Exciton liquid in coupled quantum wells. *Science* **343**, 55 (2014).

[36] Rivera, P. *et al.* Observation of long-lived interlayer excitons in monolayer $MoSe_2$-WSe_2 heterostructures. *Nat. Commun.* **6**, 6242 (2015).

[37] Miller, B. *et al.* Long-Lived Direct and Indirect Interlayer Excitons in van der Waals Heterostructures. *Nano Lett* **17**, 5229 (2017).

[38] Rivera, P. *et al.* Interlayer valley excitons in heterobilayers of transition metal dichalcogenides. *Nat. Nanotechnol.* **13**, 10041015 (2018).

[39] Forg, M. *et al.* Cavity-control of interlayer excitons in van der Waals heterostructures. *Nat. Commun.* **10**, 3697 (2019).

[40] Jauregui, L. A. *et al.* Electrical control of interlayer exciton dynamics in atomically thin heterostructures. *Science* **366**, 870 (2019).

[41] Wang, G. *et al.* Colloquium: Excitons in atomically thin transition metal dichalcogenides. *Rev. Mod. Phys.* **90**, 021001 (2018).

[42] Kang, J. *et al.* Band offsets and heterostructures of two-dimensional semiconductors. *Appl. Phys. Lett* **102**, 012111 (2013).

[43] Gong, C *et al.* Band alignment of two-dimensional transition metal dichalcogenides: Application in tunnel field effect transistors. *Appl. Phys. Lett.* **103**, 053513 (2013).

[44] Fang, H. *et al.* Strong interlayer coupling in van der Waals heterostructures built from single-layer chalcogenides. *Proc. Natl. Acad. Sci. U.S.A.* **111**, 6198 (2014).

[45] Heo, H. *et al.* Interlayer orientation-dependent light absorption and emission in monolayer semiconductor stacks. *Nat. Commun.* **6**, 7372 (2015).

[46] Alexeev, E. M. *et al.* Resonantly hybridized excitons in moir superlattices in van der Waals heterostructures. *Nature* **567**, 8186 (2019).

[47] Tran, K. *et al.* Evidence for moir excitons in van der Waals heterostructures. *Nature* **567**, 7175 (2019).

[48] Nayak, P. K. *et al.* Probing Evolution of Twist-Angle-Dependent Interlayer Excitons in $MoSe_2/WSe_2$ van der Waals Heterostructures. *ACS Nano* **11**, 4041-4050 (2017).

[49] Seyler, K. L. *et al.* Signatures of moir-trapped valley excitons in $MoSe_2/WSe_2$ heterobilayers. *Nature* **567**, 6670 (2019).

[50] Jin, C. *et al.* Observation of moir excitons in WSe_2/WS_2 heterostructure superlattices. *Nature* **567**, 7680 (2019).

[51] Wang, Z. *et al.* Evidence of high-temperature exciton condensation in two-dimensional atomic double layers. *Nature* **574**, 76 (2019).

[52] Tang, Y. *et al.* WSe_2/WS2 moir superlattices: a new Hubbard model simulator. arXiv:1910.08673 (2019).

[53] Shimazaki, Y. *et al.* Moir superlattice in a $MoSe_2$/hBN/$MoSe_2$ heterostructure: from coherent coupling of inter- and intra-layer excitons to correlated Mott-like states of electrons. arXiv:1910.13322 (2019).

[54] Regan, E. C. *et al.* Optical detection of Mott and generalized Wigner crystal states in WSe_2/WS_2 moir superlattices. arXiv:1910.09047 (2019).

[55] Bakr, W. *et al.* A quantum gas microscope for detecting single atoms in a Hubbard-regime optical lattice. *Nature* **462**, 74 (2009).

[56] Sherson, J. F. *et al.* Single-atom-resolved fluorescence imaging of an atomic Mott insulator. *Nature* **467**, 68 (2010).

[57] Kremser, M. *et al.* Discrete Interactions between a few Interlayer Excitons Trapped at a $MoSe_2$-WSe_2 Heterointerface. arxiv.org:1907.08815 (2019).

[58] Li, W. *et al.* Dipolar interactions between field-tuneable, localized emitters in van der Waals heterostructures. arxiv.org:1910.08139 (2019).

[59] Blackmore, J. A. *et al.* Ultracold molecules for quantum simulation: rotational coherences in CaF and RbCs. *Quantum Sci. Technol.* **4**, 014010 (2019).

[60] Jones, A. M. *et al.* Optical generation of excitonic valley coherence in monolayer WSe_2. *Nat. Nanotechnol.* **8**, 634 (2013).

[61] Mitioglu, A. A. *et al.* Optical manipulation of the exciton charge state in single-layer tungsten disulfide. *Phys. Rev. B* **88**, 245403 (2013).

[62] Palacios-Berraquero, C. *et al.* Large-scale quantum-emitter arrays in atomically thin semiconductors. *Nat. Commun.* **8**, 15093 (2017).

[63] Barbone, M. *et al.* Charge-tuneable biexciton complexes in monolayer WSe_2. *Nat. Commun.* **9**, 3721 (2018).

[64] Jin, C. *et al.* Identification of spin, valley and moir quasi-angular momentum of interlayer excitons. *Nat. Phys.* **15**, 1140 (2019).

[65] Branny, A. *et al.* Deterministic strain-induced arrays of quantum emitters in a two-dimensional semiconductor. *Nat. Commun.* **8**, 15053 (2017).

[66] Kurtsiefer, C. *et al.* Stable Solid-State Source of Single Photons. *Phys. Rev. Lett.* **85**, 290 (2000).

[67] He, Y.-M. *et al.* Single quantum emitters in monolayer semiconductors. *Nat. Nanotechnol.* **10**, 497 (2015).

[68] Aivazian, G. *et al.* Magnetic control of valley pseudospin in monolayer WSe_2. *Nat. Phys.* **11**, 148 (2015).

[69] Koperski, M. *et al.* Orbital, spin and valley contributions to Zeeman splitting of excitonic resonances in $MoSe_2$, WSe_2 and WS_2 Monolayers. *2D Mater.* **6**, 015001 (2019).

[70] Srivastava, A. *et al.* Optically active quantum dots in monolayer WSe_2. *Nat. Nanotechnol.* **10**, 491 (2015).

[71] Koperski, M. *et al.* Single photon emitters in exfoliated WSe_2 structures. *Nat. Nanotechnol.* **10**, 503 (2015).

[72] Chakraborty, C. *et al.* Voltage-controlled quantum light from an atomically thin semiconductor. *Nat. Nanotechnol.* **10**, 507 (2015).

[73] Glazov, M. M. *et al.* Exciton fine structure and spin decoherence in monolayers of transition metal dichalcogenides. *Phys. Rev. B*, **89**, 201302(R) (2014).

[74] Shamirzaev, T. S. *et al.* Millisecond fluorescence in InAs quantum dots embedded in AlAs. *Physica E Low Dimens. Syst. Nanostruct.* **20**, 282 (2004).

[75] Jiang, C. *et al.* Microsecond dark-exciton valley polarization memory in two-dimensional heterostructures. *Nat. Commun.* **9**, 18 (2018).

[76] Feierabend, M. *et al.* Impact of strain in the optical fingerprint of monolayer transition-metal dichalcogenides. *Phys. Rev. B*, **96**, 045425 (2017).

[77] Zhang, X. *et al.* Flux method growth of bulk MoS_2 single crystals and their application as a saturable absorber. *Cryst. Eng. Commun.* **17**, 4026 (2015).

[78] Novoselov, K. S. *et al.* Two-dimensional atomic crystals. *Proc. Natl. Acad. Sci. U.S.A.* **30**, 10451 (2005).

[79] Casiraghi, C. *et al.* Rayleigh Imaging of Graphene and Graphene Layers. *Nano Lett.* **7**, 2711 (2007).

[80] Purdie, D. G. *et al.* Cleaning interfaces in layered materials heterostructures. *Nat. Commun.* **9**, 5387 (2018).

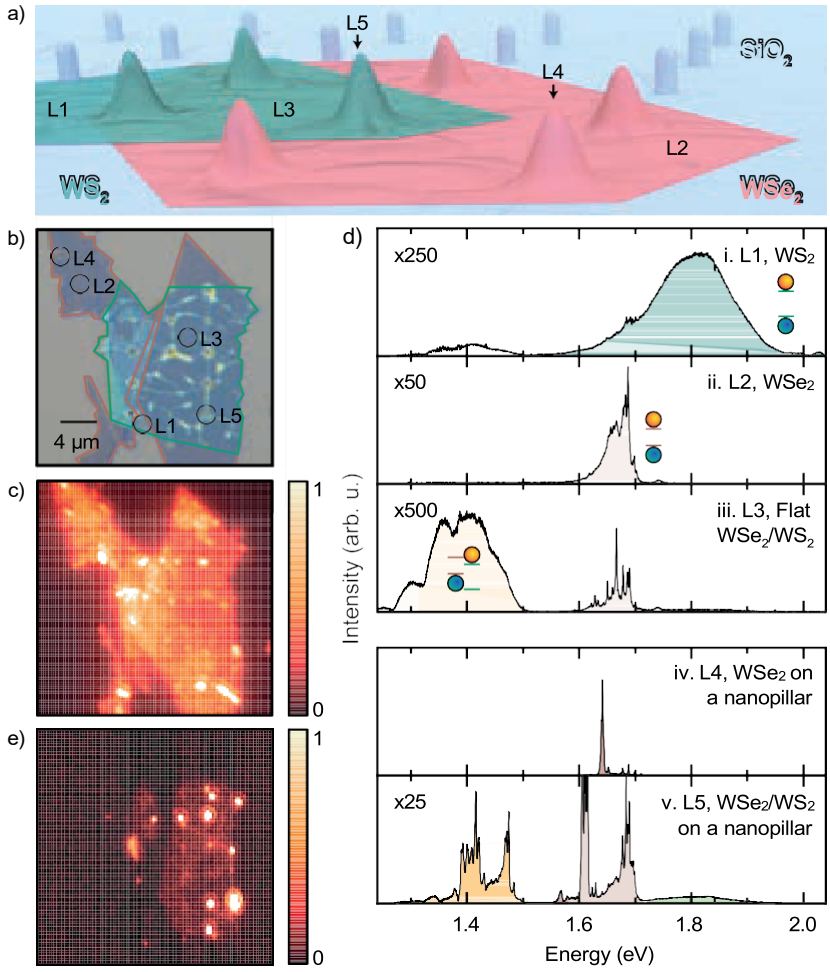

FIG. 1: **Optical characterization of the WS_2/WSe_2 heterobilayer. (a)** Illustration of our device. The SiO_2 substrate with nanopillars is in blue, the WSe_2 monolayer in red and WS_2 on top in green. Representative locations on the device are indicated: location L1 is the WS_2 monolayer, location L2 is the WSe_2 monolayer, location L3 is the flat WS_2/WSe_2 heterobilayer, location L4 is the WSe_2 monolayer on a nanopillar and location L5 is the WS_2/WSe_2 heterobilayer on a nanopillar. **(b)** Optical image of our device. WSe_2 and WS_2 monolayers are outlined in red and green, respectively. **(c)** Integrated PL intensity map of our device under 2.33-eV CW excitation at T=4 K. **(d)** Representative PL spectra under 2.33-eV CW excitation taken at the five locations highlighted in panel b. The colour coding indicates the origin of PL emission, where green (red) comes from intralayer excitons in WS_2 (WSe_2) monolayer, and yellow comes from interlayer excitons in the WS_2/WSe_2 heterobilayer. The multiplicative factors of each PL spectrum are all referenced to subpanel (iv), WSe_2 monolayer spectrum at L4. **(e)** PL intensity map of our device under 1.50-eV CW excitation at T=4 K, to which only the heterobilayer regions contribute.

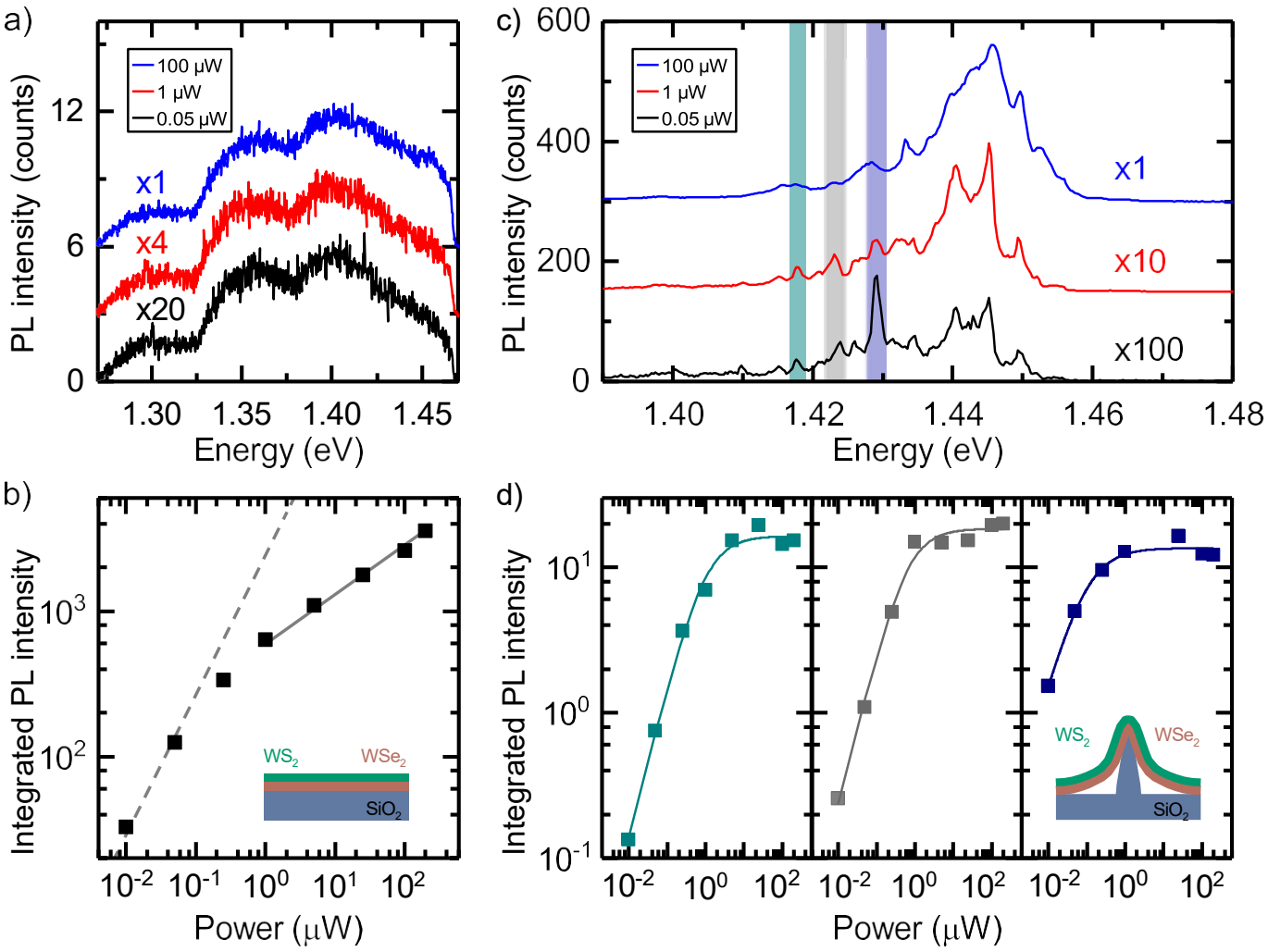

FIG. 2: **Excitation-power dependence of interlayer exciton emission. (a)** PL spectra at T=4 K from the flat heterobilayer under 1.50-eV excitation at 0.05 μW (black curve), 1 μW (red curve) and 100 μW (blue curve). **(b)** Spectrally integrated PL intensity of interlayer exciton emission as a function of excitation power, P. The dashed grey curve follows a linear dependence in P, while the solid grey curve follows $P^{0.3}$. **(c)** PL spectra from the heterobilayer on a nanopillar at 0.05-μW (black curve), 1-μW (red curve) and 100-μW (blue curve) excitation. **(d)** Spectrally integrated PL intensity of the three peaks shaded with green, grey and blue bands in panel c as a function of P. Data (filled squares) are colour-coded to the spectral bands of panel c. Solid curves are fits to data using the saturation function $A \times P^n/(P_{sat} + P^n)$, from where we determine n=0.94±0.12, 1.06±0.08 and 1.04±0.06 and saturation powers of 0.1, 0.6, and 0.9 μW for the green, grey and blue data, respectively.

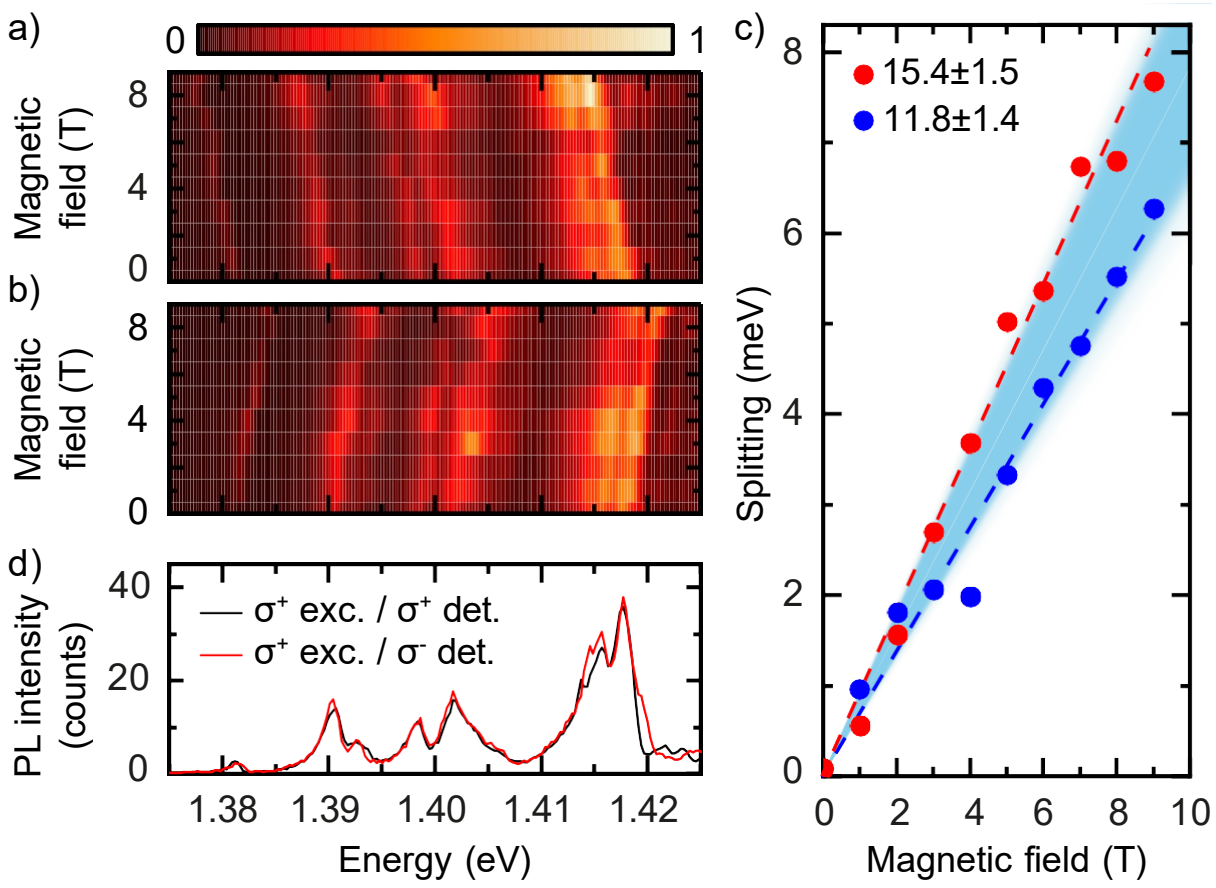

FIG. 3: **Magnetic-field dependence of trapped interlayer excitons. (a)** PL spectrum at T=4 K as a function of magnetic field B on a nanopillar under linearly polarised excitation and circularly polarised σ^+ detection. **(b)** Same measurement as panel a, but with σ^- polarised detection. The intensity of the components in a increases with B, and the blue-shifting components in b decrease with B, consistent with exciton thermalisation of Zeeman states at T=4 K[63]. **(c)** Measured Zeeman splittings of trapped interlayer excitons as a function of B. The red (blue) circles correspond to trapped interlayer excitons with the largest (smallest) g-factor of 15.4±1.5 (11.8±1.4) extracted from the linear fits (dashed curves). The mean g-factor value of all measured splittings is 13.2 with a standard deviation 1.1. When considering spin, valley and orbital contributions to the total magnetic moment, the measured range for the g-factor matches that of an exciton comprising an electron and a hole residing in different valleys[69]. **(d)** PL spectra of trapped interlayer excitons collected on the same nanopillar as panels a and b at 0 T for σ^+-polarised excitation and co-polarised (σ^+) and cross-polarised (σ^-) detection, shown as black and red curves, respectively.

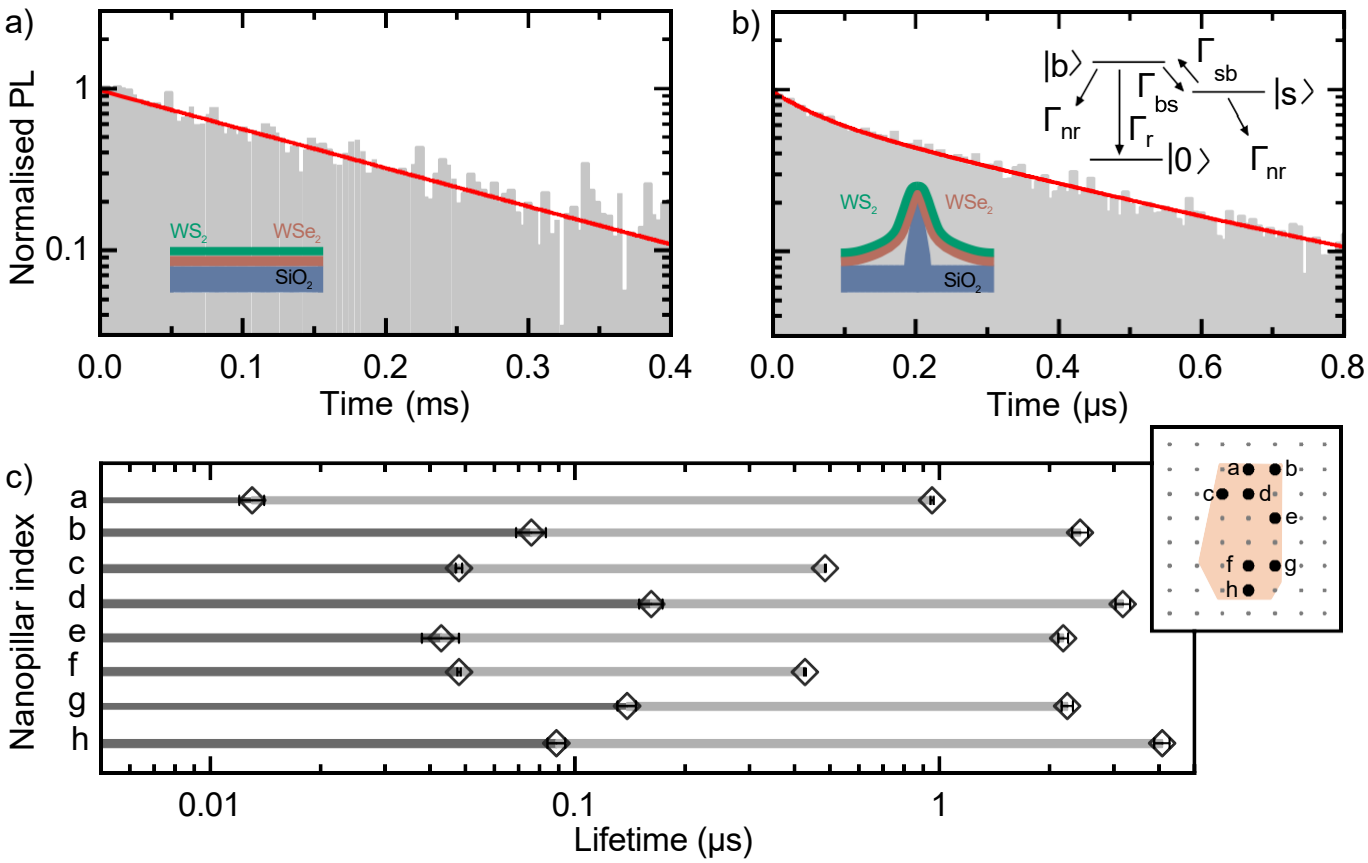

FIG. 4: **Interlayer exciton lifetime. (a)** Lifetime measurement of interlayer exciton in the flat heterobilayer region at T=4 K. The data are fitted by a single exponential (solid red curve) with a lifetime τ =180.6±3.5 μs. **(b)** Lifetime measurement of an example nanopillar-trapped interlayer exciton (1.39-eV peak from Fig. 3d). The solid red curve is a biexponential fit with two lifetimes τ_s =59.4±0.9 ns and τ_l =389.1±1.2 ns. The inset presents a three-level model with coupling between a bright state $|b\rangle$ and a shelving state $|s\rangle$, as discussed in Section 5 of the SI. **(c)** τ_s (dark grey bars) and τ_l (light grey bars) values extracted from biexponential fits to the lifetime measurements at the eight nanopillar locations (indexed a-h). The average value of τ_s (τ_l) across all nanopillars is 80 ns (2 μs). The inset maps the physical location of the nanopillars on the heterobilayer region of our device.